Multi-Dimensional Mechanical Properties Approach to Analyzing Thin UHPFRC Decks

Mengying Liu[1], Xu Li[1], Abba Auwal[1] and Fengkun Cui[2,*]

[1] School of Civil Engineering and Architecture, Linyi University, Linyi, 276000, China

[2] Department of Civil Engineering, Shandong Jiaotong University, Jinan, 250357, China

INFORMATION

Keywords:
Nonlinear numerical simulation
thin UHPFRC bridge decks
multi-dimensional model
flexural behavior

DOI: 10.23967/j.rimni.2025.10.68545

SCIPEDIA Revista Internacional de Métodos Numéricos para Cálculo y Diseño en Ingeniería

Revista Internacional Métodos numéricos para cálculo y diseño en ingeniería RIMNI CIMNE

Multi-Dimensional Mechanical Properties Approach to Analyzing Thin UHPFRC Decks

Mengying Liu[1], Xu Li[1], Abba Auwal[1] and Fengkun Cui[2,*]

[1]School of Civil Engineering and Architecture, Linyi University, Linyi, 276000, China

[2]Department of Civil Engineering, Shandong Jiaotong University, Jinan, 250357, China

ABSTRACT

This study evaluates the flexural behavior of an Ultra high performance fiber-reinforced concrete (UHPFRC) slab through experimental and Finite Element Method (FEM) analytical investigations. A full-size U-UHPFRC bridge deck specimen serves as a reference for the research. A nonlinear FEM is put forward to link material characteristics, failure mode, and bearing capacity of U-UHPFRC decks, considering the failure behavior with different impact parameters of reinforcement ratio, thickness and side ratio. The flexural performance calculation formula for UHPFRC slabs was derived using three failure modes. The results indicate that this method can effectively predict the load transfer and distribution patterns of UHPFRC thin slabs, providing a reference range for the reinforcement ratio, thickness and long-short side ratio in UHPFRC one-way or two-way slabs. These research results can optimize the crack resistance and toughness of thin UHPFRC decks, improve durability, and appropriately reduce carbon emissions. It is suitable for bridges or special structures with higher load requirements and provides theoretical support for the full-life operation and development of UHPFRC components.

OPEN ACCESS

Received: 31/05/2025

Accepted: 10/07/2025

Published: 27/11/2025

DOI
10.23967/j.rimni.2025.10.68545

Keywords:
Nonlinear numerical simulation
thin UHPFRC bridge decks
multi-dimensional model
flexural behavior

1 Introduction

Ultra-high performance fiber-reinforced concrete (hereinafter referred to as UHPFRC) exhibits self-consolidation, extremely high compressive strength, and excellent durability [1,2]. The excellent performance of UHPFRC is achieved through its dense microstructure and short-cut steel fibers [3,4], which are widely used in thin decks. On the one hand, the presence of concrete decks can significantly improve the flexural stiffness before cracking. Conventional concrete struggles with crack resistance and is prone to cracking [5–7]. On the other hand, once the concrete cracks, the stress on the bridge deck increases sharply, accelerating the degradation of the concrete. Therefore, the development of fully prefabricated UHPFRC slabs can resolve the problem of insufficient applicability of existing slabs in the bending resistance and durability of the overall structure [8–10]. The application of UHPFRC in bridge structures not only solves problems such as downward deflection of the main span and beam cracking but also realizes diverse, lightweight, and thin-walled structural forms, lowering the overall

*Correspondence: Fengkun Cui (204118@sdjtu.edu.cn).

life cycle cost of the structure. This aligns with modern bridge development concepts such as low-carbon, environmental protection, beauty and economy [11,12]. The structural system learn in this article is mainly used in the field of bridge engineering to provide high strength, high durability, and lightweight advantages [13,14]. The specific expected uses include: as a repair and reinforcement cover layer for existing concrete bridge decks, it is used as a panel element for new bridge structures and to enhance the reinforced concrete performance in composite structures; the wet connection of UHPC between prefabricated floor slabs to improve the overall integrity and seismic performance of the floor slab system under lateral seismic loads [15].

For the mechanical properties, the mechanical properties of UHPFRC slabs differ from those of ordinary concrete slabs due to the influence of steel fibers. Previous research has shown that clarifying the mechanical properties of UHPFRC wet connections, shear key construction, and loading mode impacts the failure mechanism of wet connections [15]. UHPFRC square plates with different thicknesses can be used in structures that cannot use reinforced concrete due to their light self-weight, as it was found that UHPFRC thin plate has high compressive strength and good ductile bending response [16,17]. Therefore, it is necessary to establish a mechanical method for predicting and evaluating the bending behavior of UHPFRC thin plates throughout the entire failure process. The UHPFRC plate was also subjected to negative bending moment zone tests, which improved the thickness and shear connection performance of the UHPFRC plate [18]. In terms of computational analysis and FEM, the existing theoretical analysis formulas for ordinary concrete slabs cannot accurately represent the actual results of UHPFRC slabs, and it is necessary to derive a formula that conforms to the theory for UHPFRC thin decks. In the early stages, scholars have carried out research on UHPFRC components and achieved certain results [19,20]. Bending performance tests on high reinforcement UHPFRC plates with different steel fiber volume content, tensile mechanical properties research on gridded enhanced UHPFRC sheet were conducted [21,22], and gave the bending capacity formula [23]. UHPFRC Waffle bridge panels were analyzed for the bending, shear performance and the influence of major design parameters through finite element and tests [24,25]. Large-scale UHPFRC beams were used in bending test research on the deformation and bearing capacity [26], and a multi-layer analysis model of prestressed UHPFRC was constructed to calculate the bearing capacity [27]. In addition, previous research has shown that the process from loading to failure of a UHPFRC slab is a nonlinear one [28]. A nonlinear numerical model of a reinforced UHPFRC composite beam was established to verify the reinforcement effect of using reinforced UHPFRC as a bridge deck pavement, and the composite beam was analyzed for its structural response and cracking [29–31]. By conducting nonlinear analysis on the strain of UHPFRC corresponding to influencing factors, a basis is provided for the design of UHPFRC thin plate partitioning principles.

This paper conducts a multidimensional analysis of UHPFRC thin decks, focusing on component size, nonlinearity, and structural performance. The study evaluates a full-size U-UHPFRC bridge deck test, from the elastic state to failure. Proposes a theoretical analysis model for positive torque before failure, and establishes a nonlinear numerical model to investigate the relationship between tensile strain and material properties during the failure process of UHPFRC. It compares the results of theoretical analysis and numerical simulation with the calculation results of an ordinary high-strength concrete slab. Variable parameter analyses the factors affecting the mechanical properties of UHPFRC thin plates. This provides a reference for guiding the UHPFRC thin deck design.

2 Experimental Studies and Nonlinear Numerical Analysis

2.1 Speciment

The full-scale model test was conducted in the Key Laboratory for Structural Safety Maintenance of the Federal Polytechnic University of Lausanne, Switzerland. The UHPFRC used in the components was a specially designed UHPFRC by the MCS laboratory, which is a premixed type with a base composed of cement, silica fume, and sand. The steel fiber content can reach 3%, resulting in high mechanical properties [32,33]. The purpose of this experiment was to study the stress behavior of U-shaped bridge decks, and the test results are shown in Fig. 1.

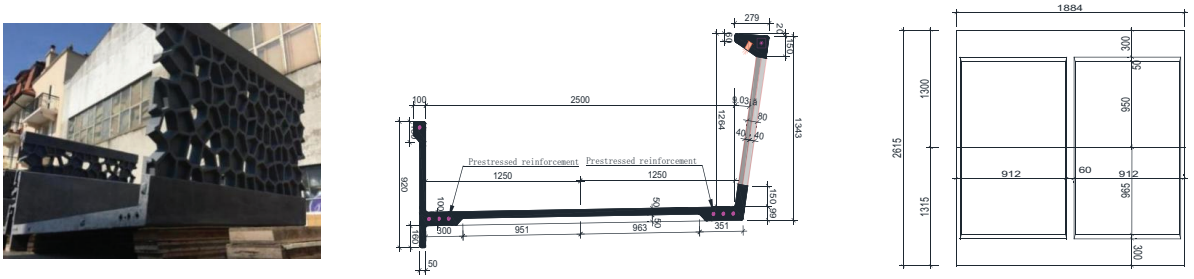

(**a**) (**b**) (**c**)

Figure 1: The specimen (unit: mm): (**a**) Complete view; (**b**) Side view; (**c**) Top view

2.2 Test and Instrumentation

Fig. 2a–e shows the three-point bending test setup. Rigid steel blocks are used for simple support, and strip-shaped wooden blocks are placed between the steel beam and the test model. The load is applied by the actuator at the middle span. Fig. 2f,g shows the top deflection measured by five measuring instruments (D1∼D5), and four measuring instruments (S1∼S4) are used to measure the bottom deflection. Nine transverse and longitudinal strain gauges in the sample for strain measurement. R1∼R5 are UHPFRC bottom rib strain gauges. L1∼L2 and T1∼T2 are used to measure the longitudinal and transverse strains at the bottom of the specimen, respectively.

2.3 Structure Discretization Analysis

The experimental results are compared with the theoretical results to verify the correctness of the numerical model. The solid element is used to simulate UHPFRC and ordinary high-strength concrete slabs, while steel bars are simulated using the rod element. The hexahedron is the main grid division method, the FEM is shown in Fig. 3.

2.4 Constitutive Relation

The UHPFRC constitutive model in FEM adopts the full strain fracture model, where the compression characteristic function is the Thorenfeldt function, and the tensile constitutive model uses a multiline function to simulate the entire stress-strain process, as shown in Fig. 4a,b. Ordinary high-strength concrete (C60) slabs are selected for comparison, with the same model size [34]. The constitutive model of C60 is simulated using a constant model, as shown in Fig. 4c,d. Ordinary steels use the Von Mises model. The elastic modulus of UHPFRC, C60 and steel bar are 50 GPa, 36 GPa, and 205 GPa, respectively. Specific material characteristic parameters are given in Table 1.

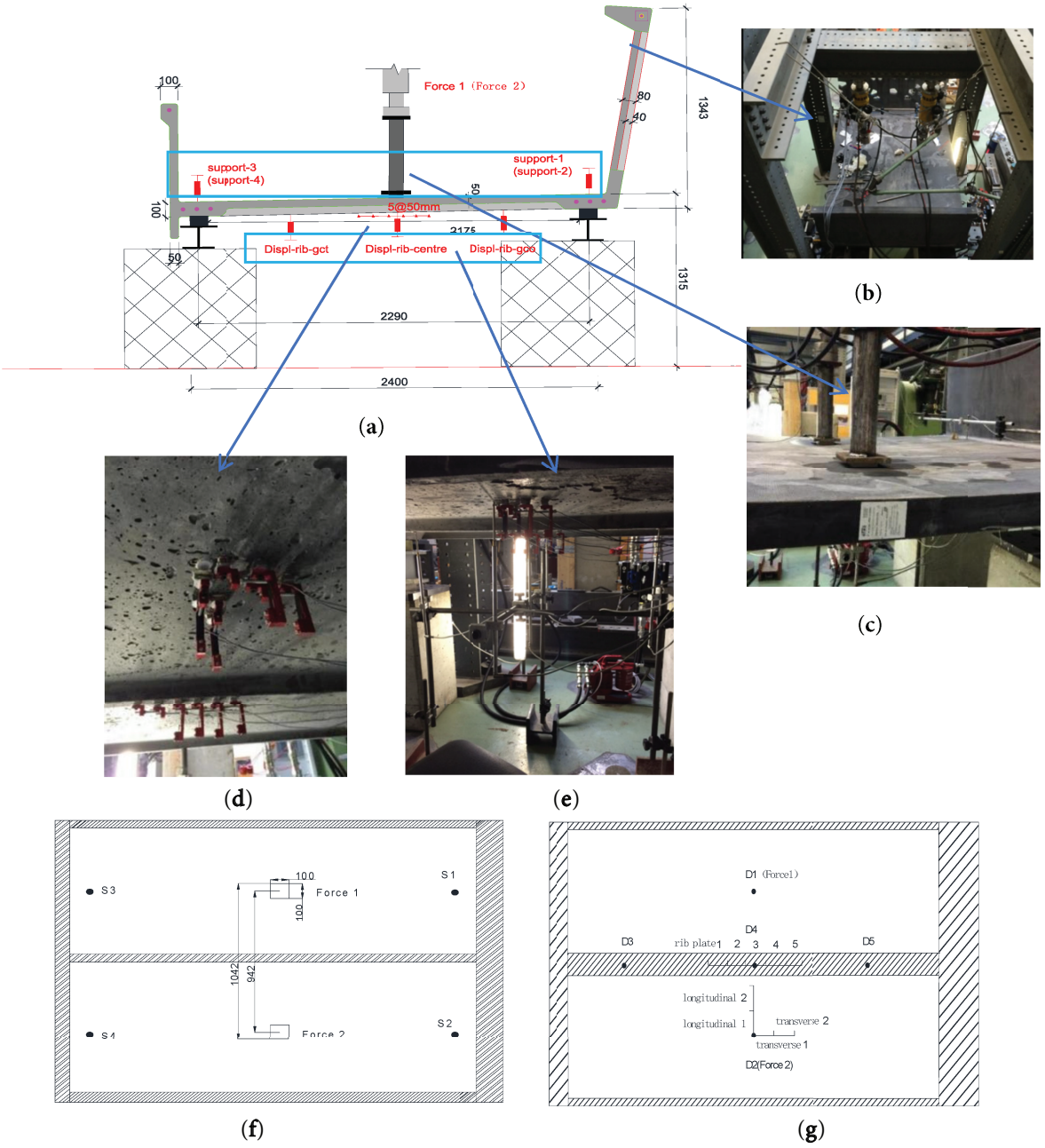

Figure 2: Test setup of (unit: mm): (a) Study model; (b) Loading position on top surface; (c) Top measuring positions; (d) Strain position on bottom; (e) Displacement transducers position on bottom; (f) Front positions; and (g) Bottom positions

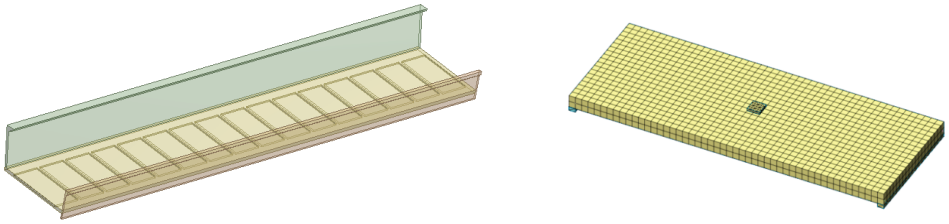

(a) (b)

Figure 3: FEM: (**a**) Full bridge model; (**b**) Local beam model

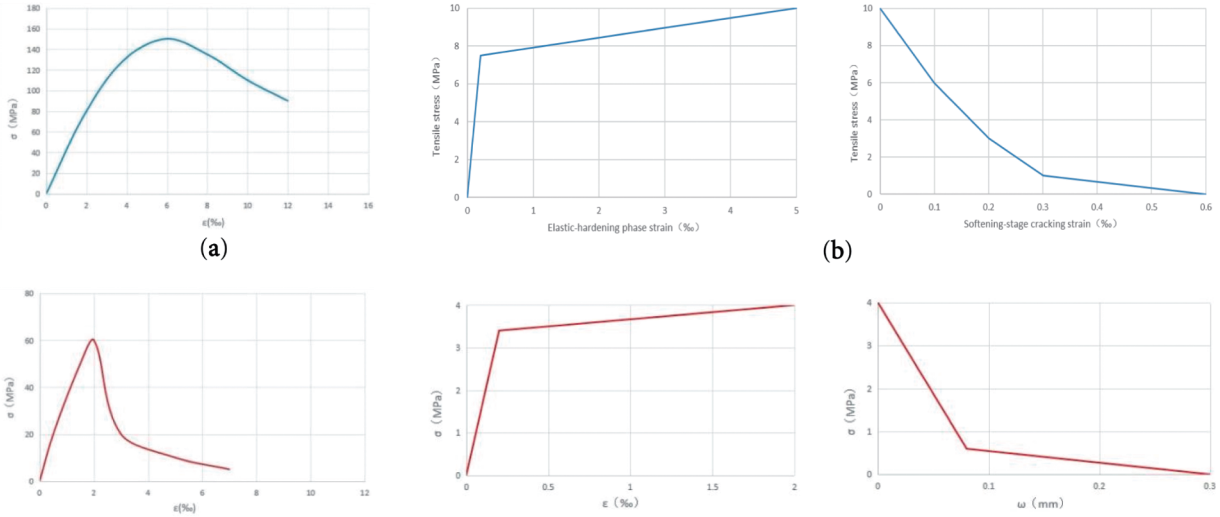

(a) (b) (c) (d)

Figure 4: Constitutive model:(**a**) UHPFRC compression; (**b**) UHPFRC tensile; (**c**) C60 compression; (**d**) C60 tensile

Table 1: Material characteristic parameters

UHPFRC	f_{Ute} (MPa)	f_{Utu} (MPa)	ε_{Ute} (‰)	ε_{Uts} (‰)	ε_{Utu} (‰)	f_{Ucu} (MPa)	E_U (GPa)
	6.5	10	0.15	2.0	5.0	150	50
Ordinary steels	f_{sy} (MPa)	f_{su} (MPa)	ε_{sy} (‰)	ε_{sy} (‰)	E_s (GPa)	ϕ (mm)	N
	500	510	2.19	100	205	14	2
Prestressed steels	f_{sy} (MPa)	f_{su} (MPa)	ε_{sy} (‰)	ε_{su} (‰)	E_s (GPa)	ϕ (mm)	N
	760	1860	2.19	100	195	15.2	6

2.5 Load Simulation

A set of nodes is set vertically on both sides to simulate the boundary conditions, limiting the displacement and angle in the x and z directions while releasing the displacement and angle in the y

direction. To reduce local stress concentration and avoid local punching damage caused by excessive load, nodes are set at the center of the finite element to simulate the loading of steel plates. Finally, the descending section curve along the normal direction of the loading block is obtained using displacement load control.

2.6 Result Analysis

As shown in Fig. 5a, the center displacement of the 1/2 U-shaped beam calculated by the nonlinear FEM is compared with the center displacement under the action of forces 1 and 2 obtained from experiments. The trend of the three curves is the same, consistent with the test load-displacement curves, obtained under two types of concentrated forces, especially when the displacement is less than 10 mm. Fig. 5b shows the load-strain curves the trend of lateral load-strain variation is in good agreement with the experimental strain law, especially for the two strain curves of measuring point force 2, which almost overlap. Therefore, the established nonlinear FEM can simulate actual stress well. In the test UHPFRC-U beam, cracks appeared at the subsurface bottom plate, and the first visible crack appeared at the central rib, eventually forming several visible longitudinal and vertical cracks. The maximum vertical crack was connected with a longitudinal crack. The failure mode is shown in Fig. 6.

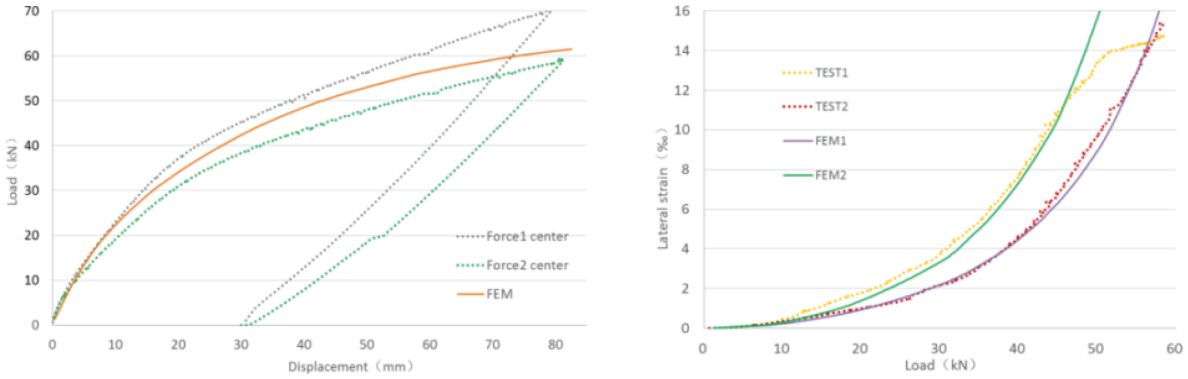

(**a**) (**b**)

Figure 5: The comparison of the test and FEM: (**a**) Load-displacement curves; (**b**) Load-strain curves

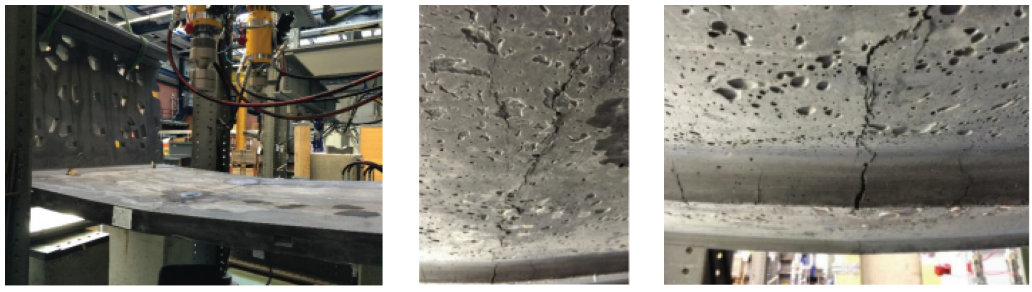

(**a**) (**b**) (**c**)

Figure 6: Failure modes of the U-beam test: (**a**) Top surface failure of the bottom plate; (**b**) Bottom surface failure of the bottom plate;(**c**) Bottom rib failure

3 Nonlinear Theoretical Calculation

Taking the experimental model as a reference., assume the length, width, and displacement of the slab are L, B and δ, respectively, as shown in Fig. 7a. According to the nonlinear characteristics of UHPFRC material, when a concentrated load is applied to a slab, the possible ductile slab failure modes are divided into three types: I, II and III. Category II can be divided into two modes (IIa and IIb), and category III can be divided into two modes (IIIa and IIIb), thus giving five modes in total. The ultimate bearing capacity equation P_U is derived, and the ultimate bending capacity is predicted, where the bending moments of the ultimate positive and negative resistance plates are represented as m_u and $m_u^{'}$, respectively.

3.1 Failure Mode I

In this mode, the slab is destroyed along the width, and only one crack appears, as shown in Fig. 7b. The virtual work equation is given by:

$$P_{U,I} = 4m_u \frac{B}{L} \tag{1}$$

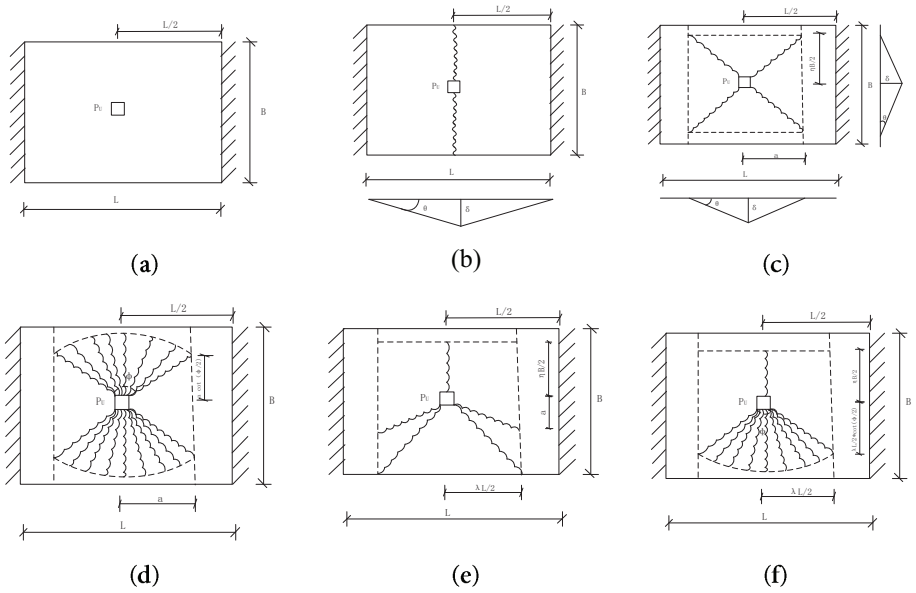

Figure 7: Theoretical analysis of failure patterns: (**a**) Two-way slab with concentrated load; (**b**) Failure pattern I; (**c**) Failure pattern IIa; (**d**) Failure pattern IIb; (**e**) Failure pattern IIIa; and (**f**) Failure pattern IIIb

3.2 Failure Mode II

Failure mode II can be divided into two parts of the yield line: IIa and IIb, as shown in Fig. 7c,d. Assume the distance of the line from the center is a, while the distance of the free edge is $\eta B/2$, where $0 < \eta \leq 1$, and the central angle is denoted by ϕ.

(1) Mode IIa

The ultimate bearing capacity is $P_{U,IIa}$, and the virtual work equation is given by:

$$P_{U,II_a} = \frac{8m_u a}{\eta B} + \frac{2\left(m_u^{'} + m_u\right)\eta B}{a} \tag{2}$$

When the minimum $P_{U,IIa}$, occurs $\frac{dP_{U,IIa}}{da} = 0$, there is

$$P_{U,II_a} = 4\left(1+\eta\right)\sqrt{m_u\left(m_u^{'} + m_u\right)} \tag{3}$$

(2) Mode IIb

The ultimate bearing capacity is $P_{U,IIb}$:

$$P_{U,II_b} = 4m_u \cot\frac{\phi}{2} + 2\left(m_u^{'} + m_u\right)\phi \tag{4}$$

When $m_u^{'} = 0$, then $\cot\frac{\phi}{2} = \sqrt{\frac{m_u^{'}}{m_u}} = 0$, $\phi = \pi$.

$$P_{U,II_a} = 4\left(1+\eta\right)\sqrt{m_u^2} = 4\left(1+\eta\right)m_u \sim (4.0, 8.0]\, m_u \tag{5}$$

$$P_{U,II_b} = 2\pi \cdot m_u = 6.28 m_u \tag{6}$$

3.3 Failure Mode III

Fig. 7e,f shows failure modes IIIa and IIIb. In mode III, there is only one yield line extending from the loading point to free edge, while several yield lines are restricted within the slab on the other side.

(1) Mode IIIa

The virtual work equation is:

$$P_{U,III_a} = \frac{4m_u}{\lambda L}\left(a + \frac{\eta B}{2}\right) + \left(m_u^{'} + m_u\right)\frac{\lambda L}{a} \tag{7}$$

When the minimum occurs $P_{U,IIIa}$, then $\frac{dP_{U,IIIa}}{d\phi} = 0$,thus,

$$P_{U,III_a} = 4\sqrt{m_u\left(m_u^{'} + m_u\right)} + \frac{\eta B}{\lambda L/2} m_u \tag{8}$$

(2) Mode IIIb

The central angle is denoted by ϕ. The virtual work equation is:

$$P_{U,III_b} = 2m_u\left(\cot\frac{\phi}{2} + \frac{\eta B}{\lambda L}\right) + \left(m_u^{'} + m_u\right)\phi \tag{9}$$

When $m_u^{'} = 0 \cot\dfrac{\phi}{2} = \sqrt{\dfrac{m_u^{'}}{m_u}} = 0, \phi = \pi$, the two sectors in failure mode IIIb are connected to form a full circle. If $a = \dfrac{\lambda L}{2}\sqrt{\dfrac{m_u^{'} + m_u}{m_u}} = 1/2\lambda L$, the loading position is at the center point $a = \dfrac{1}{2}\lambda L \le \dfrac{B}{2}$, so $\dfrac{B}{\lambda L/2} \ge 2$, then,

$$P_{U,III_a} = 4m_u + \frac{\eta B \cdot m_u}{\lambda L/2} \ge 4m_u + 2\eta m_u \sim (4.0; 6.0]\, m_u \tag{10}$$

$$P_{U,III_b} = \pi m_u + \frac{\eta B \cdot m_u}{\lambda L/2} \ge 3.14m_u + 2\eta m_u \sim (3.14; 5.14]\, m_u \tag{11}$$

When calculating the bearing capacity, the minimum load leading to failure is calculated according to different failure modes. Among them, failure mode I applies to one-way slabs, while failure modes II and III apply to two-way slabs. Based on the three failure modes under a concentrated load, the corresponding calculation formula for P_U is derived, with the boundary condition of simply supported edges at both ends, namely, $m_u^{'} = 0$. The averaging point is taken as the theoretical calculation value, and the calculation formula for the slab theoretical bearing capacity in each calculation model is shown in Table 2.

Table 2: Theoretical bearing capacity of the slab calculation expression

Failure mode	I	IIa	IIb	IIIa	IIIb
Bearing capacity P_{U1}	$4m_u\dfrac{B}{L}$	$6.00m_u$	$6.28m_u$	$5.00m_u$	$4.14m_u$

3.4 Failure Mode Verification

Fig. 8. shows the failure mode verification diagram according to the test component size.

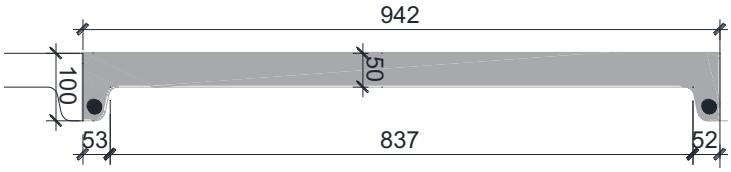

Figure 8: 1/2 longitudinal section (unit: mm)

The calculation process is as follows:

$$\alpha\frac{f_{Ucu}}{\gamma_c}xb_f = \frac{f_{Utu}}{K\gamma_c}\left(\frac{h}{2} - x\right)b_f + \frac{h}{2}\frac{f_{Utu}}{K\gamma_c}b + \frac{f_y}{\gamma_m}A_s \tag{12}$$

$$M_u = \frac{f_y}{\gamma_m}A_s\left(h_0 - \frac{x}{2}\right) + \frac{h}{4}\frac{f_{Utu}}{K\gamma_c}\left(\frac{h}{2} - x\right)b_f + \frac{h^2}{4}\frac{f_{Utu}}{K\gamma_c}b \tag{13}$$

By substituting the height of the compression zone into Eqs. (12) and (13), the ultimate bending moment per unit width can be obtained as:

$$m_u = \frac{M_u}{B} = \frac{13.41\,\text{kN}\cdot\text{m}}{0.942m} = 14.24\,\text{kN}\cdot\text{m/m} \tag{14}$$

Under normal circumstances, failure mode I plays a controlling role in one-way slabs. However, according to failure mode I, the theoretical ultimate flexural capacity of the 1/2 specimen is 21.46 kN · m, which is far from the experimental results ($F_1 = 74.8$ kN and $F_2 = 63.7$ kN), with a mean value of 69.25 kN, a difference of 69%. The experimental failure mode is similar to failure mode III, and the theoretical calculated value is 71.2 kN, with a difference of 2.7% from the experimental mean value. It can be seen that UHPFRC slabs should be designed considering the two-way slab failure mode. Moreover, the derived theoretical formula can well simulate the ultimate flexural capacity of UHPFRC slabs.

4 Parameters Comparison and Analysis

4.1 Impact Parameters

Considering the main factors affecting the bearing capacity of slabs, there are many factors influencing the structural behavior of reinforced UHPFRC slabs. The selected analysis parameters are: boundary conditions, reinforcement ratio (ρ), thickness (h), and long–short side ratio (λ). Based on the mechanical properties test specimen, two pairs of simply supported edges are selected as boundary conditions. According to the minimum reinforcement ratio [35], 0% to 1.0% is selected for ρ and increased in steps of 0.2%. The h range is 10 to 100 mm, increasing in steps of 10 mm [36,37]. The calculation parameters for λ are 1.0 to 5.0, increasing in steps of 0.5.

Taking the size of the U-beam as a reference, a single-factor analysis of the bearing capacity influence parameters of UHPFRC slabs is conducted, in which a concentrated load acting on the central point to simulate the most unfavorable condition for the bending member. Twenty-five FEMs are established to determine the bearing capacity factors. All calculation models are shown in Table 3.

Table 3: Parameters of the structural model

Reinforcement ratios										
Model no.	①	②	③	④	⑤	⑥				
ρ (%)	0.0	0.2	0.4	0.6	0.8	1.0				
Invariant	Width: 942 mm; Length: 2500 mm; h: 50 mm									
Thickness										
Model no.	①	②	③	④	⑤	⑥	⑦	⑧	⑨	⑩
h (mm)	10	20	30	40	50	60	70	80	90	100
Invariant	Width: 942 mm; Length: 2500 mm; ρ: 0.0%									
Edge length ratios										
Model no.	①	②	③	④	⑤	⑥	⑦	⑧	⑨	
Long and short sides ratio	1.0	1.5	2.0	2.5	3.0	3.5	4.0	4.5	5.0	
Width (mm)	2500	1667	1250	1000	833	714	625	556	500	
Invariant	Length: 2500 mm; ρ: 0.0%; h: 50 mm									

Under concentrated load, the theoretical value P_{U1} of the slab flexural bearing capacity corresponding to each failure mode is calculated and compared with the ultimate bearing capacity P_{U2} calculated by numerical simulation.

4.2 Contrastive Analysis

The bearing capacity difference of slabs with different parameters and the variation curves calculated by FEM and the theoretical model are shown in Figs. 9a–c and 10a–c.

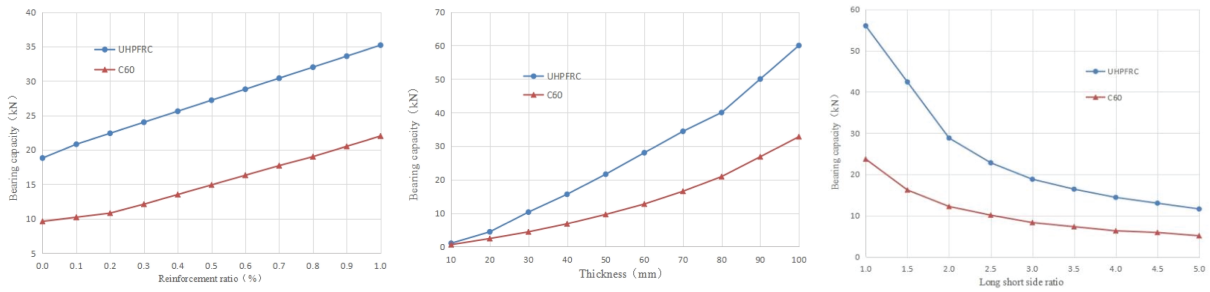

(a) (b) (c)

Figure 9: FEM bearing capacity curves with different parameters: (**a**) Reinforcement ratios; (**b**) Thickness; (**c**) Edge length ratios

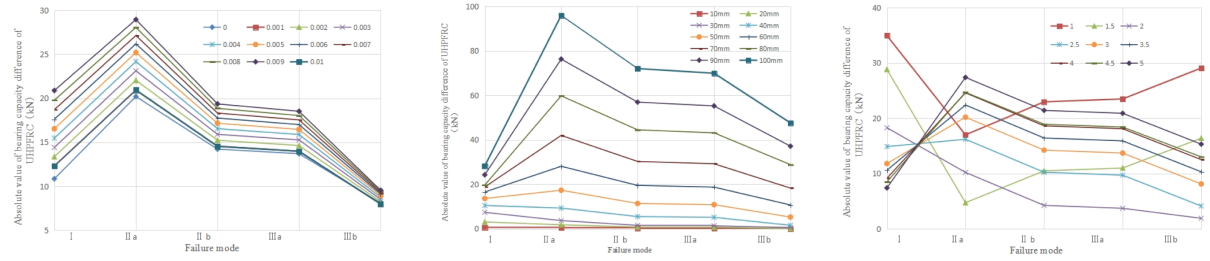

(a) (b) (c)

Figure 10: Absolute difference value distribution of bearing capacity with different parameters: (**a**) Reinforcement ratios; (**b**) Thickness; (**c**) Edge length ratios

Figs. 9a and 10a show that the longitudinal reinforcement ratio has almost no effect on the division of UHPFRC a one-way and two-way slabs. The major failure pattern is the two-way slab. With increasing ρ, the ultimate bearing capacity of the UHPFRC slab is greater than that of C60, both increasing linearly. The difference is relatively uniform, at approximately 12 kN. The failure mode of C60 with ρ less than 0.6% is the one-way failure mode I, while UHPFRC is calculated according to a two-way slab. Additionally, according to the minimum reinforcement ratio [36,37], 0.6% can be assigned as the minimum for UHPFRC two-way slabs.

Figs. 9b and 10b show that the thinner the plate, the more obvious the two-way slab effect is. The absolute difference of each failure mode increases, from 0.4 kN to 27 kN. The ultimate bearing capacity of UHPFRC is greater than that of C60. When the UHPFRC thickness is greater than 70 mm and the C60 is greater than 40 mm, they are mainly one-way failure mode I. In other cases, they are mainly manifested in the two-way failure mode III.

Figs. 9c and 10c show that the ultimate bearing capacity of both types of slabs gradually decreases, and the difference gradually decreases from 32.3 to 6.5 kN with increasing λ. The ultimate bearing capacity of the UHPFRC slab is greater than that of C60. The long-short side ratio has the most significant influence on the division of one-way and two-way slabs. The smaller the ratio of long and short sides, the more obvious the two-way slab effect is.

4.3 Strain Analysis

To further study the strain variation law of the UHPFRC slab, combined with the analysis of the effect of different parameters, long–short side ratios of 1.0 to 3.5 and thicknesses of 30 to 70 mm are selected for analysis. In Fig. 11, all strain measurement points are at the center of the slab bottom element. The horizontal axis represents the ratio of the distance between each measurement point and the center point of the numerical model to half of the transverse and longitudinal length, the smaller the ratio, the closer it is to the center point. Figs. 12 and 13 show the bottom strain variation law under various parameters along the direction of the long and short edge centerlines, respectively.

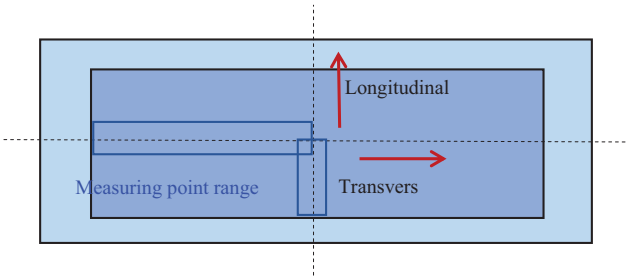

Figure 11: Strain range and direction of the bottom side

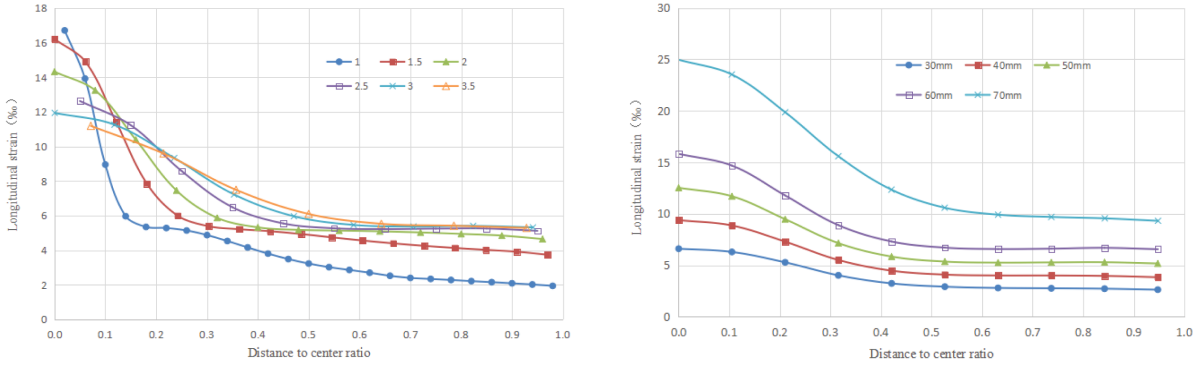

(a) (b)

Figure 12: Strain curves along the longitudinal direction: (**a**) Ratio of short and long sides varies; and (**b**) Thickness varies

(1) Longitudinal strains

Fig. 12a shows that the distribution range of cracks begins to develop along the entire longitudinal direction with increasing long-short side ratio, first increasing and then decreasing. The maximum strain value appears in the center range, and strains gradually decrease from the center to the edge until the strain curve is almost horizontal. The strain curves with long-short side ratios of 1.0 and 1.5

decrease sharply from the center point to the ranges of 0.18 (225 mm) and 0.3 (250 mm), respectively, while the decline of other strain curves is gentle. When the strain value exceeds the ultimate tensile strain value (5‰) of UHPFRC, cracks occur. For long-short side ratios take 1.0, 1.5, 2.0, 2.5, 3.0 and 3.5, the distribution ranges at 325 , 333 , 450 , 500 , 417 and 357 mm, respectively, are all greater than 5‰. When the long-short side ratio is 2.5, the range of cracks is the widest.

Fig. 12b shows that the strain variation trend in the longitudinal direction for different thicknesses is the same, and the maximum strain value of each curve appears at the center. The thicker the slab, the greater the strain value at the same position, and the strain slowly decreases from the center to the edge. As the distance to the center ratio increases, the strain curve is almost flat. When the thickness is greater than 50 mm, the strain values are greater than the ultimate tensile strain values (5‰), the strain distribution range is 471 mm, and cracks begin to develop along the entire longitudinal direction. Strain values at a thickness of 70 mm are significantly greater than those of other thicknesses. As the thickness increases, the distribution range of cracks becomes more uniform.

(2) Transverse strains

Fig. 13 shows that the maximum strain value appears at the slab loading center and then decreases rapidly, lattening out afterward. The transverse strain curves change significantly at center ratios of 0.18 and 0.14, respectively, after which they almost coincide, and the strain values hover at approximately 2‰, but they are always less than the longitudinal strain. Additionally, the strain peak with a thickness of 70 mm is the largest, and the growth is the most significant. The influence of the long-short side ratio and thickness change on the distribution of transverse cracks is smaller than that along the longitudinal direction. The crack distribution gradually concentrates toward the center, accounting for approximately 2/5 of the transverse side. The change in thickness has little effect on the distribution range of cracks at the slab bottom along the transverse direction.

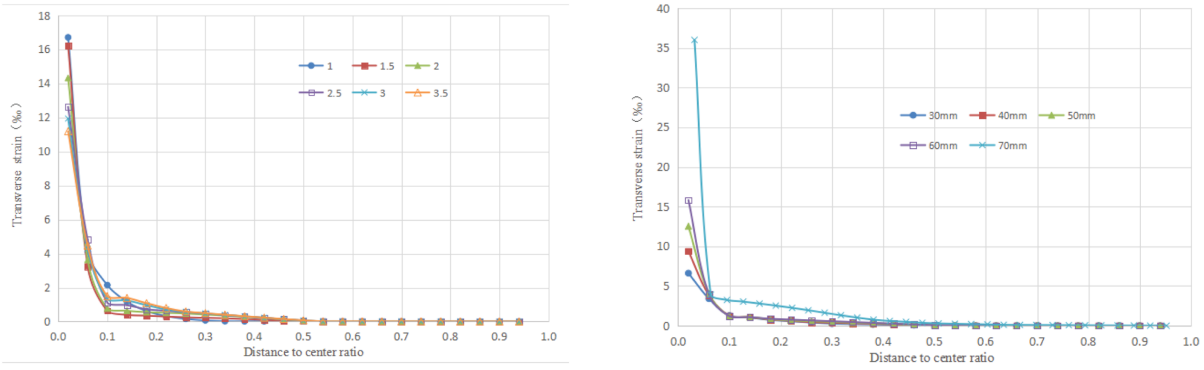

(a) (b)

Figure 13: Strain curves along the transverse direction: (**a**) Ratio of short and long sides varies; and (**b**) Thickness varies

5 Conclusion

UHPFRC, especially components made of UHPFRC, not only solves the inherent limitations of traditional concrete but also pushes UHPFRC into a new field of durability and strength. Based on this, the research conclusions of this article are as follows:

(1) A universal expression for the flexural bearing capacity of UHPFRC plates with universal physical significance has been established. The characteristic value of bearing capacity can be directly obtained by the critical value of bending moment per unit width. A unified mechanical model for the bearing capacity of UHPFRC thin decks in three failure modes (I, II, III) has been established. Failure mode I is one-way slab failure, and modes II and III are two-way slab failure.

(2) According to the displacement and cracking states of the U-bridge deck, the bearing capacity and strains of the entire process can be extracted from the nonlinear FEM representing UHPFRC thin slabs. The main material characteristic parameters in FEM are also given. Based on the nonlinear model, UHPFRC slabs have better bending resistance than C60 due to the addition of steel fibers and the interaction between UHPFRC and reinforcements, which effectively restricts crack development and significantly improves the flexural capacity, overall stiffness, and deformation capacity of UHPFRC slabs.

(3) The division principles for UHPFRC one-way and two-way slabs were obtained. The failure of UHPFRC slabs is mainly manifested in failure mode IIIb of two-way slabs. The long-short side ratio has the greatest influence on the division of UHPFRC one-way and two-way slabs, followed by thickness, and then reinforcement ratio. It is suggested that when the long-short side ratio is less than or equal to 3.5, UHPFRC slabs should be calculated as two-way slabs; when the ratio is greater than 3.5, they should be calculated as one-way slabs. The thicker the slab, the more obvious the one-way slab effect, and the thinner the two-way slab effect. When the thickness is less than 70 mm, the UHPFRC slab should be calculated as a two-way slab. It is suggested to take 0.5% as the minimum reinforcement ratio of UHPFRC two-way slabs.

(4) The strains of UHPFRC slabs change significantly along the longitudinal direction and are always greater than those along the transverse direction, indicating longitudinal bending failure. In addition to the rapid growth of strain at the central slab point, the variation range along the longitudinal direction is much larger than that along the transverse direction. The strains change more intensely with different long-short side ratios than with various thicknesses, mainly along the longitudinal direction.

Acknowledgement: None.

Funding Statement: This research was funded by the Application of Intelligent Management Evaluation Technology in Engineering Quality, Safety and Environmental Protection, grant number 29024266.

Author Contributions: The authors confirm contribution to the paper as follows: Conceptualization, methodology, software and funding acquisition, Mengying Liu; formal analysis and writing, Abba Auwal; investigation, Xu Li; resources and data curation, Fengkun Cui. All authors reviewed the results and approved the final version of the manuscript.

Availability of Data and Materials: The data that support the findings of this study are available from the Corresponding Author, [Fengkun Cui], upon reasonable request.

Ethics Approval: Not applicable.

Conflicts of Interest: The authors declare no conflicts of interest to report regarding the present study.

References

1. Shao X, Sun X, Zou D, Cao J, Yang C. Research on an innovative structure of an open-ribbed steel-ultra-high performance concrete composite bridge deck. Front Struct Civ Eng. 2024;18(5):716–30. doi:10.1007/s11709-024-1053-7.
2. Chen Y, Tong J, Li Q, Xu S, Shen L. Application of high-performance cementitious composites in steel-concrete composite bridge deck systems: a review. J Intell Constr. 2024;2(2):1–23. doi:10.26599/jic.2024.9180012.
3. Xiao R, Song C, Sun B, Guo R, Chen H. Design and experimental study of a replaceable steel-UHPC composite bridge deck. Structures. 2022;40(1):1107–20. doi:10.1016/j.istruc.2022.04.091.
4. Çiftçioğlu AÖ, Kazemi F, Shafighfard T. Grey wolf optimizer integrated within boosting algorithm: application in mechanical properties prediction of ultra high-performance concrete including carbon nanotubes. Appl Mater Today. 2025;42(289):102601. doi:10.1016/j.apmt.2025.102601.
5. Liu Y, Zhang Q, Bao Y, Bu Y. Fatigue behavior of orthotropic composite deck integrating steel and engineered cementitious composite. Eng Struct. 2020;220(1):111017. doi:10.1016/j.engstruct.2020.111017.
6. Shan Y, Gong Y, Wang Y, Zhou Q, Li X, Ding F, et al. Flexural behavior of ultra-high performance concrete (UHPC) shaped thin-plate ribbed staircases: an experimental and numerical study. Mater Struct. 2024;57(1):18. doi:10.1617/s11527-023-02282-x.
7. Zha S, Deng W, Liu D, Zhang J, Gu J. Experimental study on flexural behavior of steel-laminated concrete (NC and UHPC) composite beams with corrugated steel webs. Eng Struct. 2024;306(11):117802. doi:10.1016/j.engstruct.2024.117802.
8. Ghasemi S, Mirmiran A, Xiao Y, Mackie K. Accelerated testing of super lightweight UHPC waffle deck under heavy vehicle simulator. Bridge Struct. 2021;16(2–3):61–74. doi:10.3233/brs-200176.
9. Liu J, Chen Z, Guan D, Lin Z, Guo Z. Experimental study on interfacial shear behaviour between ultra-high performance concrete and normal strength concrete in precast composite members. Constr Build Mater. 2020;261(6):120008. doi:10.1016/j.conbuildmat.2020.120008.
10. Shen X, Brühwiler E, Peng W. Biaxial flexural response of strain-hardening UHPFRC circular slab elements. Constr Build Mater. 2020;255:119344. doi:10.1016/j.conbuildmat.2020.119344.
11. Jabbar A, Danha L, Hasan Q. Numerical simulation of ultra-high-performance concrete's compressive and tensile behaviour in beams. J Appl Eng Sci. 2023;21(2):532–46. doi:10.5937/jaes0-40769.
12. Xue J, Briseghella B, Huang F, Nuti C, Tabatabai H, Chen B. Review of ultra-high performance concrete and its application in bridge engineering. Constr Build Mater. 2020;260(6):119844. doi:10.1016/j.conbuildmat.2020.119844.
13. Qiu M, Shao X, Yan B, Zhu Y, Chen Y. Flexural behavior of UHPC joints for precast UHPC deck slabs. Eng Struct. 2022;251(2):113422. doi:10.1016/j.engstruct.2021.113422.
14. Yang J, Xia J, Zhang Z, Zou Y, Wang Z, Zhou J. Experimental and numerical investigations on the mechanical behavior of reinforced concrete Arches strengthened with UHPC subjected to asymmetric load. Structures. 2022;39(31–32):1158–75. doi:10.1016/j.istruc.2022.03.087.
15. Wang H, Li S, Liu X. Experimental study on the tensile-shear coupling performance of fully prefabricated assembled floor slabs with UHPC wet connections. Case Stud Constr Mater. 2025;22(6):e04457. doi:10.1016/j.cscm.2025.e04457.
16. Wang Q, Yang M, Wang X, Liu H, Zhou C, Jiang C. Study of ultra-high-performance concrete containing multivariate supplementary cementitious materials: experiments and modeling. Fuller Nanotub Carbon Nanostruct. 2023;31(6):549–58. doi:10.1080/1536383X.2023.2189239.
17. Spasojevic A, Redaelli D, Muttoni A. Thin UHPFRC slabs without conventional reinforcement as lightweight structural elements. In: Proceedings of the Concrete: 21th Century Superhero Fib Symposium; 2009 Jun 22–24; London, UK. doi:10.5075/epfl-thesis-2930.

18. Sharifa AM, Assi NA, Al-Osta M. Use of UHPC slab for continuous composite steel-concrete girders. Steel Compos Struct. 2023;34:321. doi:10.12989/SCS.2020.34.3.321.
19. Wang Z, Song L, Gao C, Wang J, Zhang S, Su W, et al. Cyclic loading test of self-centering precast segmental concrete high-speed railway bridge columns with UHPC-filled duct connections. Eng Struct. 2023;293(6):116507. doi:10.1016/j.engstruct.2023.116507.
20. Hu Y, Meloni M, Cheng Z, Wang J, Xiu H. Flexural performance of steel-UHPC composite beams with shear pockets. Structures. 2020;27(11):570–82. doi:10.1016/j.istruc.2020.05.039.
21. Zhou Z, Zhang Y, Wang YQ, Han FY, Tian HW, Peng Z. Experimental study on tensile mechanical propery of grid reinforced UHPC plates. J Southeast Univ Nat Sci Ed. 2019;49(4):611–7. (In Chinese).
22. Zhao Q, Yang M, Li C. Experimental research on the bending resistance of hruhpc slabs with different steel fiber volumes. Ind Constr. 2018;48(10):148–51,125. (In Chinese). doi:10.13204/j.gyjz201810025.
23. Zhan J, Nussbaumer A, Brühwiler E. Influence of fiber orientation on the high cycle tensile fatigue resistance of Ultra-High Performance Fiber Reinforced Cementitious Composites (UHPFRC). Int J Fatigue. 2024;180(2):108103. doi:10.1016/j.ijfatigue.2023.108103.
24. Zhu JS, Wang YG, Yan JB, Guo XY. Shear behaviour of steel-UHPC composite beams in waffle bridge deck. Compos Struct. 2020;234(5):111678. doi:10.1016/j.compstruct.2019.111678.
25. Pang K, Zhou H, Wu C, Jiang H, Zhang Z, Yu Y, et al. Study on behavior of waffle-type UHPC-GFRP composite slab under three-point loading. Case Stud Constr Mater. 2023;19:e02457. doi:10.1016/j.cscm.2023.e02457.
26. Wang L, Bi J, Liu L, Xiao Z. Flexural properties of low-height prestressed T-beams: tests and numerical simulations. Int J Struct Integr. 2024;15(1):120–45. doi:10.1108/ijsi-07-2023-0058.
27. Cafarelli R, Accornero F, Carpinteri A. Size-scale effects in high-performance reinforced and prestressed concrete T-beams. Struct Concr. 2023;24(5):5649–63. doi:10.1002/suco.202200673.
28. Semendary AA, Svecova D. Factors affecting bond between precast concrete and cast in place ultra high performance concrete (UHPC). Eng Struct. 2020;216(10):110746. doi:10.1016/j.engstruct.2020.110746.
29. Yang IH, Joh C, Kim BS. Structural behavior of ultra high performance concrete beams subjected to bending. Eng Struct. 2010;32(11):3478–87. doi:10.1016/j.engstruct.2010.07.017.
30. Sleiman E, Ferrier E, Michel L, Saidi M. Seismic behavior of masonry-infilled reinforced concrete frames strengthened using ultra-high performance concrete diagonal strips. Structures. 2024;59(1):105790. doi:10.1016/j.istruc.2023.105790.
31. Cao Q, Wang X, Wu Z, Gao R, Jiang X. Flexural behavior of carbon fiber-reinforced polymer partially bonded reinforced concrete beams with different anchorage methods. ACI Struct J. 2024;121(1):61–74. doi:10.14359/51739185.
32. Rambabu D, Sharma SK, Akbar MA. Performance evaluation of ultra-high performance concrete (UHPC) and ultra-high performance fibre reinforced concrete (UHPFRC) in pavement applications. Arab J Sci Eng. 2024;49(10):13685–707. doi:10.1007/s13369-024-08771-7.
33. Shen X, Brühwiler E. Biaxial flexural fatigue behavior of strain-hardening UHPFRC thin slab elements. Int J Fatigue. 2020;138:105727. doi:10.1016/j.ijfatigue.2020.105727.
34. Shen X, Brühwiler E. Influence of local fiber distribution on tensile behavior of strain hardening UHPFRC using NDT and DIC. Cem Concr Res. 2020;132(2):106042. doi:10.1016/j.cemconres.2020.106042.
35. Chinese Standard (GB 50010-2010). Code for design of concrete structures. Beijing, China: China Construction Industry Press; 2014. (In Chinese).
36. Technical Leaflet SIA 2052. UHPFRC—materials, design and construction. Zurich, Switzerland: Swiss Society of Engineers and Archtitects; 2016.
37. Chinese Standard (JTG D60-2015). General specifications for design of highway bridge and culverts. Beijing, China: People's Communications Press; 2015.